Volume 7 | Number 37 | 7 October 2019 | Pages 11317–11652

Journal of Materials Chemistry C

Materials for optical, magnetic and electronic devices

rsc.li/materials-c

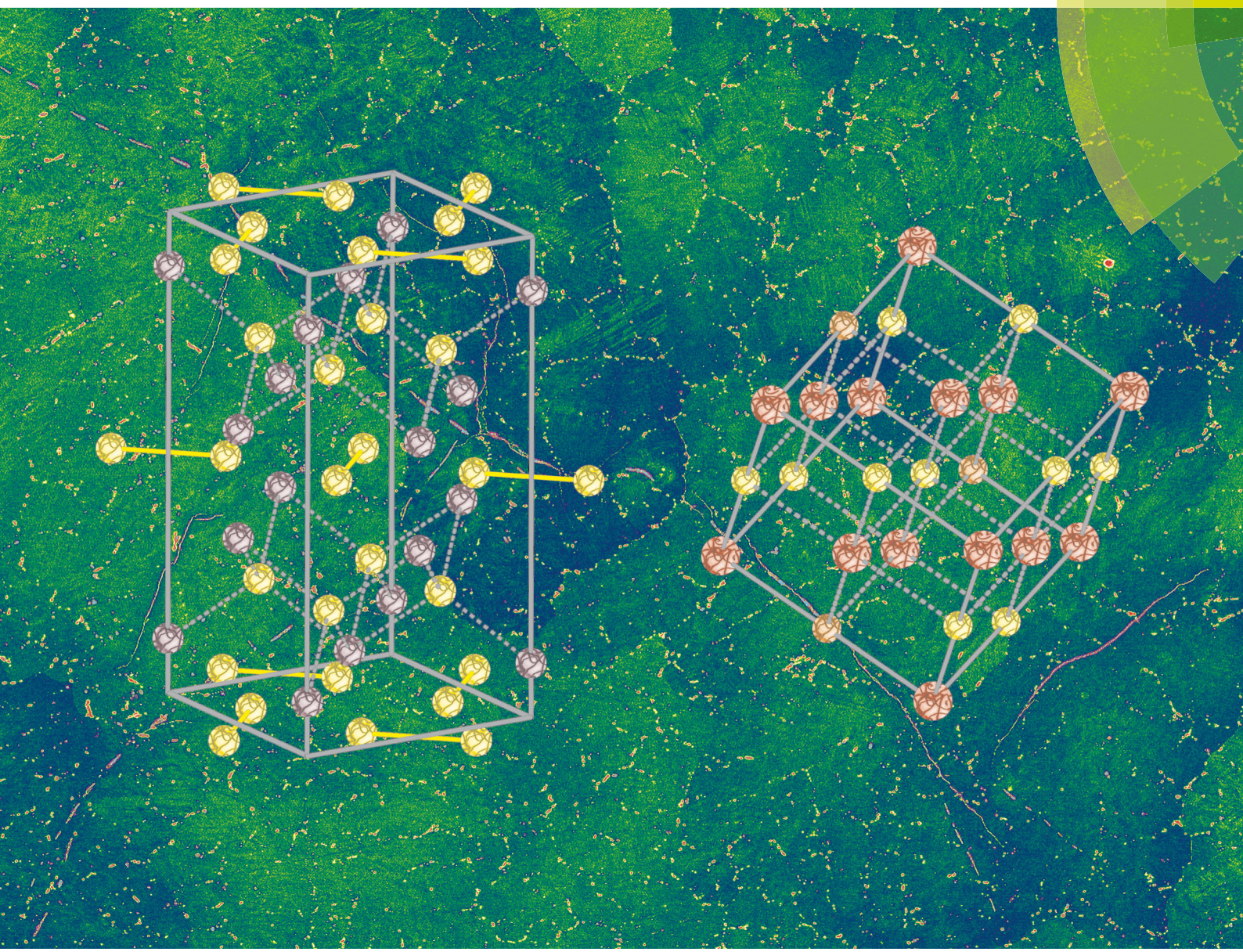

ISSN 2050-7526

ROYAL SOCIETY OF CHEMISTRY | Celebrating IYPT 2019

PAPER

Oliver Oeckler *et al.*

Cobalt germanide precipitates indirectly improve the properties of thermoelectric germanium antimony tellurides

Journal of Materials Chemistry C

PAPER

View Article Online
View Journal | View Issue

Cite this: J. Mater. Chem. C, 2019, 7, 11419

Cobalt germanide precipitates indirectly improve the properties of thermoelectric germanium antimony tellurides†

Daniel Souchay,[a] Stefan Schwarzmüller,[a] Hanka Becker,[b] Stefan Kante,[b] G. Jeffrey Snyder,[c] Andreas Leineweber[b] and Oliver Oeckler *[a]

Different established synthesis methods such as melt-casting followed by annealing as well as melt-spinning or ball-milling followed by hot-pressing or spark plasma sintering may significantly influence the properties of thermoelectric materials. The comparison of microstructures obtained by different synthesis routes (water-quenching and melt-spinning followed by spark plasma sintering) reveals the indirect nature of the beneficial influence of cobalt germanide precipitates on the thermoelectric properties of germanium telluride and germanium antimony tellurides (GST materials). Cobalt germanide precipitates significantly influence the thermoelectric properties of GST materials: the thermoelectric figure of merit zT of $(GeTe)_{17}Sb_2Te_3$ obtained by quenching melts in water increases from 1.6 to 1.9 (at 450 °C) by introducing cobalt germanide precipitates. They drastically reduce the grain and sub-grain sizes of the GST matrix. Melt-spinning followed by spark plasma sintering leads to nanoscopic cobalt germanide precipitates, whose effect on the thermoelectric properties, especially the phononic thermal conductivity, surprisingly seems to be marginal. This is due to the already significantly reduced (sub-)grain sizes in such polycrystalline GST samples as revealed by orientation ("channeling") contrast in backscattered-electron micrographs. Melt-spun and spark-plasma-sintered GST material exhibits similar thermoelectric figures of merit zT values as water-quenched samples with cobalt germanide precipitates. In addition to providing easier access to samples with small (sub-)grains by simple quenching, the precipitates may stabilize the GST or GeTe microstructure by Zener pinning as cobalt is insoluble in the matrix material. This is very favorable concerning cyclability during thermoelectric measurements and potential applications. The heterostructured materials and their thermoelectric properties are long-term stable. Hall effect measurements of heterostructured GST (melt-spun and spark-plasma-sintered) indicate that the charge carrier concentration is near optimum.

Received 24th June 2019,
Accepted 16th August 2019

DOI: 10.1039/c9tc03410b

rsc.li/materials-c

Introduction

Germanium antimony tellurides $(GeTe)_nSb_2Te_3$ (GST materials) have become well-known as the most prominent class of phase-change materials for non-volatile random access memory and optical data storage media.[1–5] GST materials exhibit fast crystallization kinetics combined with high electrical conductivity and low thermal conductivity.[6–8] The latter transport properties are also beneficial for thermoelectric materials.[6]

Thermoelectric generators that convert waste heat to electrical energy may contribute to establish a multitude of sensors such as thermostatic radiator valves, transmitters, light sensors or aircraft monitoring,[9,10] which require only a few hundred micro- or milliwatts to operate. Thus, only small temperature differences are necessary to make them autonomous as no cables or battery changes are necessary if they have access to waste heat.[11] In addition, thermoelectric generators can provide independent energy supply in places where no other form of electricity is available, *e.g.* using thermoelectric generators in ventilators for stoves[12] or in space missions.[11] Thermoelectric materials may thus contribute to sustainable and renewable energy management, *e.g.* combining thermoelectric generators with salinity gradient solar pond, photovoltaic systems or by harvesting the waste heat of hot spring thermal energy.[13,14]

[a] Institute for Mineralogy, Crystallography and Materials Science, Faculty of Chemistry and Mineralogy, Leipzig University, Scharnhorststr. 20, 04275 Leipzig, Germany. E-mail: oliver.oeckler@gmx.de
[b] Institute of Materials Science, TU Bergakademie Freiberg, Gustav-Zeuner-Str. 5, 09599 Freiberg, Germany
[c] Department of Materials Science and Engineering, Northwestern University, Evanston, IL 60208, USA

† Electronic supplementary information (ESI) available: Details of syntheses and sintering, density and Dulong-Petit C_p values, powder X-ray diffraction patterns, scanning and transmission electron microscopy (including EDX and SAED), and thermoelectric measurements. See DOI: 10.1039/c9tc03410b

Many thermoelectric materials are being explored for such power generation applications, such as chalcogenides,[15] *e.g.* germanium telluride co-doped with BiTe and Cu with a zT value (see below) up to 1.55 in the temperature range of 325 to 450 °C,[16] or PbTe co-doped by Na and Cl with Na on cation sites providing additional electrons to the conduction band, resulting in a zT value of 1.27 at 375 °C.[17] Other recent examples include $Pb_xSn_{1-x}Te$ alloys, where Bi_2Te_3 doping increases zT in the low-temperature range (210 to 340 °C) compared to pristine $Pb_xSn_{1-x}Te$ samples,[18] as well as silicides[15] such as higher manganese silicides exhibiting textured behavior leading to ~10% zT enhancement parallel to the pressing direction. Such anisotropic behavior in non-cubic polycrystalline thermoelectric materials should be carefully considered.[19] Concerning the rather isotropic half-Heusler compounds, *e.g.* doping $Ti_{0.3}Zr_{0.35}Hf_{0.35}NiSn$ with Sb and/or Bi increases in zT value up to 0.58 at 550 °C.[20]

However, research for optimized thermoelectric materials faces several problems, especially their thermal stability and their rather low efficiency. The latter depends on the dimensionless figure of merit $zT = S^2\sigma T/(\kappa_e + \kappa_{ph})$, where κ_e and κ_{ph} are the electronic and phononic thermal conductivities, respectively, S the Seebeck coefficient, σ the electrical conductivity and T the temperature. In spite of the seemingly simple equation, the individual transport properties contributing to zT are highly correlated: σ depends on the charge carrier density n and the mobility μ according to $\sigma = ne\mu$ (Drude model).[21] High S would be beneficial for high zT values and requires a high effective mass m^* according to $S = (8\pi^2 k_B^2\, m^* T)\,(\pi/3n)^{2/3}\,(3eh^2)^{-1}$, assuming a parabolic band model with energy independent scattering approximation.[22] However, a high m^* would mean low μ according to $\mu = e\tau/m^*$ (τ = scattering relaxation time) which results in a low σ. High σ, on the other hand, results in high total thermal conductivity κ according to the Wiedemann–Franz law $\kappa e\sigma^{-1} = LT$ (L = Lorenz number).[23] A decrease in L is correlated with an increase in thermopower, *i.e.* the absolute value of Seebeck coefficient according to $L = 1.5 + e^{(-|S|/116)}$ (where L is in 10^{-8} W Ω K^{-2} and S in μV K^{-1}).[24] This equation is a good approximation when a single parabolic band is applicable and when acoustic phonon scattering dominates. κ_{ph} is one parameter which can be influenced by real-structure effects such as domain boundaries or nanoscale precipitates. However, the energy range of long-wavelength acoustic phonon modes has to be in the same range as the presumed phonon scattering centers as shown for *e.g.* skutterudites.[25] The so-called phonon-glass electron-crystal (PGEC) concept[26] focuses on disorder and "rattling" atoms that may enhance phonon scattering by reducing the mean free path of phonons, whereas σ ideally remains almost unaffected if electron or hole conduction is associated with the rigid framework.

The free path distribution range of phonons and thus the thermal conductivity may further be reduced by micro- or nanoscaled side phases in heterostructured systems.[27] For example, such secondary phases in GST materials such as elemental germanium[28] or antimony[29] have been shown to increase zT significantly. Endotaxially intergrown nanoinclusions of SrTe in PbTe lead to peak zT values up to ~2.2 at 640 °C.[30] LAST (Pb–Sb–Ag–Te) thermoelectric materials obtained by quenching melts exhibit Ag–Sb-rich nanoscale inclusions with coherent or semicoherent interfaces in a PbTe-rich matrix; and further nanoscale inclusions related to compositional fluctuations of Ag, Sb and Pb/Sn have been described in the system $Ag(Pb_{1-y}Sn_y)_mSbTe_{2+m}$.[31,32] Such decrease in lattice thermal conductivity has, however, also been explained by solid solution effects, *e.g.* for PbTe alloyed with MgTe[33] and strain effects in PbTe with nanoinclusions of SrTe.[34]

Instead of nano- and micro-inclusions of second phase, pronounced real structure effects in chemically homogeneous GST materials are also beneficial concerning their thermoelectric properties.[6,35–39] Compounds $(GeTe)_nSb_2Te_3$ with $n \geq 3$ exhibit a disordered rocksalt-type high-temperature modification. Quenching this phase affords a metastable pseudocubic modification with short-range vacancy ordering and herringbone-like twinned nanostructures. The planar defects present reduce thermal conductivity drastically, most likely by scattering long-wavelength phonons.[38,40] For $n < \sim 12$, the stable room temperature (RT) phases correspond to long-periodically ordered layered structures that consist of rocksalt-type building blocks separated by van der Waals gaps. Increasing the GeTe content to $n \geq 12$ leads to materials that can be considered as doped variants of GeTe. In the GST class of materials, many elements are suitable for substitution, *e.g.* Mn,[41] Sn,[42] Cd,[43] Li,[44,45] Ag,[46] or Cr[47] replacing Ge; As[48] or In[49,50] replacing Sb, and Se[35] replacing Te. These substitutions change the electronic structure and charge carrier density and thus influence the thermoelectric performance.

Comparable to GST composite materials (see above), some heterostructured variants of GeTe exhibit high zT values. $Ge_{0.87}Pb_{0.13}Te$[51] with zT = 1.9 at 500 °C and $Ge_{0.87}Pb_{0.13}Te$ with 3 mol% Bi_2Te_3[52] (zT = 1.9 at 500 °C) both contain PbTe-rich domains as a side phase. The heterostructured material with the nominal composition $Ge_{0.9}Sb_{0.1}Te_{0.9}Se_{0.05}S_{0.05}$[53] represents an Sb-doped $GeTe_{1-x}Se_x$ matrix containing $GeS_{1-x}Se_x$ precipitates. By substituting Te in GeTe with Se and S, κ_{ph} was reduced by phonon scattering due to mass fluctuations. As an effect of spark plasma sintering, κ_{ph} was further reduced by alloying with Sb, which leads to additional point defects and grain boundaries. However, these heterostructured samples combine substitution of the matrix material with additional precipitates, which makes it difficult to trace individual effects.

Furthermore, the microhardness of such precipitate-containing samples is increased compared to GeTe.[53] In general, heterostructuring affects mechanical properties by maintaining the microstructure, which is well-known *e.g.* for δ-ferrite precipitates in steel.[54] Grain-boundary migration can be impeded by small particles, an effect known as Zener pinning.[55,56] Such particles generate a pinning pressure as it is energetically unfavorable to move past the particle because new boundaries must be created. This counteracts the driving force pushing the boundaries during annealing (mainly the energy stored by grain boundary curvature, especially at high-angle grain boundaries). This aspect is highly relevant for thermoelectric materials with respect to maintaining the microstructure and thus ensuring long-term performance.

In order to study the influence of precipitates in GST materials, a composition close to the optimal charge carrier concentration is

most relevant. As precipitates should not influence the GST material by substitution, cobalt germanides are a particularly good choice as cobalt is almost insoluble in GeTe [57] and GST with cobalt-rich precipitates.[58,59] Thus, this is an optimal model system to analyze the effect of precipitates on thermoelectric properties. Comparing $(GeTe)_nSb_2Te_3$ with different values of n with and without cobalt germanide precipitates is an intriguing way to elucidate the influence of precipitates on thermoelectric properties. Since good thermoelectric properties for GST with 1 wt% of $CoGe_2$ precipitates had been demonstrated, these compositions served as basis for this study.[58] Different synthesis routes such as quenching in water compared with melt-spinning (MS) followed by spark plasma sintering (SPS) allow for comparing more or less coarse microstructures.

Experimental

Synthesis

Bulk samples were obtained by fusing ~3 g (water-quenched samples) and ~10 g (MS/SPS samples) of the elements Co (smart elements, 99.98%), Ge (Haines & Maassen 99.999%), Sb (VEB Spurenmetalle Freiberg, 99.9999%), and Te (Haines & Maassen 99.9%) in silica glass ampules under dry Ar atmosphere at 950 °C for at least 8 hours and quenching the melts at air (for MS/SPS) or in water (water-quenched). The water-quenched samples were annealed at 590 °C for 24 h, again followed by quenching in water. Ingots for MS and SPS were induction-melted in a custom-built melt-spinner using silica-glass tubes with a round nozzle measuring 1 mm in diameter. The tube and its surrounding were constantly flushed by inert Ar gas (Fig. S1, ESI†). Immediately after a sample was completely remolten, the melt was ejected onto a rotating copper wheel. The wheel speed, nozzle-wheel gap and ejection pressure were 1500 rpm, 0.3 mm and 0.35 bar (Ar overpressure), respectively. The obtained flakes (approximately 8 g) were placed in a 12 mm diameter graphite die and densified using an SPS apparatus (HDP25, FCT Systeme, Germany) by heating to 475 °C with 100 K min^{-1} and holding this temperature for 15 min with an uniaxial pressure of 70 MPa (more details given in Table S1, ESI†). Chemical compositions of all samples are listed in Table S2, ESI.† Disc-shaped specimens for thermal conductivity measurements and cuboid slabs of the same samples for measurements of the electrical resistivity and the Seebeck coefficient were sawn out from the SPS pellets or water-quenched ingots using a diamond wire saw and polished with SiC grinding powder until they were plane-parallel.

Analytical methods

X-ray diffraction. For RT powder X-ray diffraction (PXRD), crushed samples on flat specimen holders were measured on a Huber G670 diffractometer (Guinier geometry with imaging-plate detector and integrated read-out system) with Cu-$K_{\alpha1}$ radiation [Ge(111) monochromator, λ = 1.54051 Å]. WINXPOW[60] was used for evaluation of PXRD data and TOPAS[61] for Rietveld refinements. Reflection profiles were described using a direct convolution approach with fundamental parameters. Stephens' model was used to fit anisotropic peak broadening.[62] The background of each diffraction pattern was fitted by a set of 10 parameters (shifted Chebychev polynomial). Temperature-dependent measurements of samples in rotating silica glass capillaries under dry Ar atmosphere were recorded on a similar device with Mo-$K_{\alpha1}$ radiation [Ge(220) monochromator, λ = 0.71093 Å] equipped with a ceramic heating fork.

Electron microscopy

Scanning electron microscopy (SEM) and energy-dispersive X-ray spectroscopy (EDX) were done using a Zeiss LEO 1530 Gemini instrument (acceleration voltage 20 kV) equipped with an EDX detector (INCA software,[63] Oxford Instruments). Microstructural investigations were carried out using polished (final stage: colloidal silica suspension; OP-S, Struers) cross sections perpendicular to the disc plane of the samples using the orientation contrast (''channeling'') of backscattered electron (BSE) for imaging.

Selected-area electron diffraction (SAED), high resolution transmission electron microscopy (HRTEM) and further EDX measurements were executed on a Philips CM-200 STEM (LaB_6 cathode, 200 kV, super-twin lens, point resolution 0.23 nm) equipped with an RTEM 136-5 EDX detector (EDAX, Genesis[64] software). A double-tilt low-background sample holder (Gatan) was used. For TEM investigations, the bulk material was manually cut, mechanically polished using a dimple grinder (Gatan) and then Ar-ion-thinned (Duo-Mill, GATAN). Evaluation of SAED data was done using the Analysis[65] software. For HRTEM and SAED simulations, jEMS[66] was used.

Transport properties

Thermal diffusivity was measured on samples with thicknesses of 0.7–1.75 mm under He atmosphere with a Linseis LFA 1000 apparatus equipped with an InSb detector. Simultaneous heat loss and finite pulse corrections were applied using Dusza's model.[67] Values were averaged from five measurement points at each temperature. For the calculation of κ (= κ_e + κ_{ph}), they were multiplied with the Dulong-Petit heat capacity and the density as derived by the weight and the volume determined by Archimedes' principle with a precision of 0.03 g cm^{-3}. Previous work has shown that the heat capacities of several GST materials[28,35,38] agree well with the Dulong-Petit values. Details on heat capacities and densities (all >98.5% of the X-ray densities) are given in Table S2, ESI.† S and σ were measured simultaneously under He atmosphere with a Linseis LSR-3 instrument with NiCr/Ni and Ni contacts and a continuous reversal of the polarity of the thermocouples (bipolar setup). Measurements comprised three heating/cooling cycles between 50 °C and 500 °C with 25 °C steps at 10 K min^{-1} heating rate; a temperature gradient of 50 K was applied and three data points were acquired per temperature. All samples were polycrystalline (see Fig. 1 and Fig. S12, ESI†) with the dimensions of 1.51–2.02 mm × 1.55–2.5 mm × 7.21–8.84 mm; there is no evidence for pronounced preferred orientation. This is corroborated by the fact that no significant deviation in transport properties

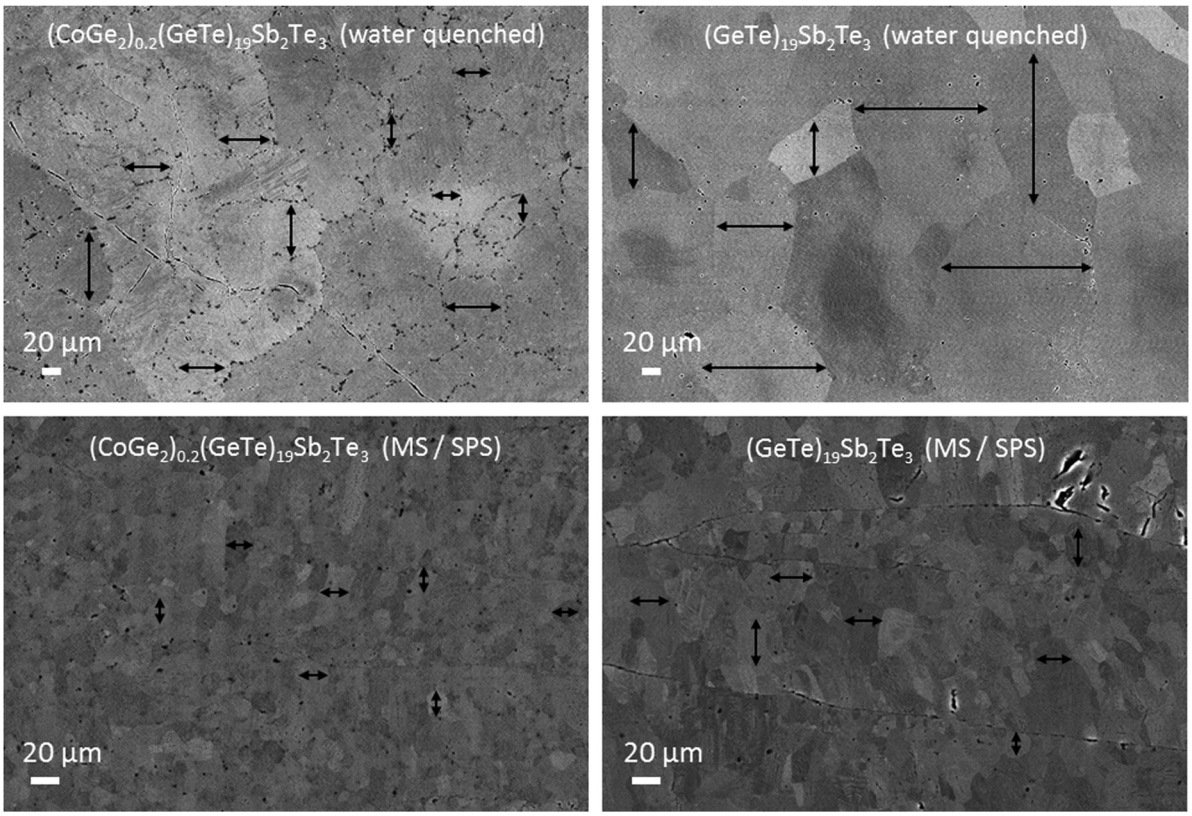

Fig. 1 SEM-BSE images of water-quenched (top) and MS/SPS (bottom) heterostructured samples containing a $(GeTe)_{19}Sb_2Te_3$ matrix and cobalt germanide precipitates (left) and pristine $(GeTe)_{19}Sb_2Te_3$ (right) after thermoelectric measurements (three cycles up to 500 °C); dark gray spots correspond to cobalt germanides mainly located at grain or sub-grain boundaries of the GST matrix in water-quenched samples; in all images, the microstructure of GST is clearly visible due to orientation ("channeling") contrast of backscattered electron (black arrows visualize the different grain and/or sub-grain sizes). Note that small dots with white halos correspond to pores whereas dark dots represent cobalt germanides (mainly visible in the left top image).

was detected when measuring vertical or horizontal to press direction of the SPS samples (Fig. S2, ESI†). The errors of S and σ are smaller than 10%; respectively for κ, they are approximately 5%. The combined absolute uncertainty of the measurements may amount up to 15% for the zT values. For further characterization, Hall measurements were carried out under dynamic vacuum applying a magnetic field of 2 T and currents of 100 mA. Using the van der Pauw technique, metal contacts were fixed onto the samples by screws.[68]

Results and discussion

Phase composition and crystal structures

In order to evaluate the influence of the cobalt germanide precipitates on the thermoelectric properties, GeTe was compared with two corresponding heterostructured materials that formally contain 1 wt% $CoGe_2$ or 1 wt% Co_5Ge_7 according to the nominal composition, assuming that Co is insoluble in the GST matrix. Samples obtained by MS and SPS were compared with water-quenched ones annealed 1 day at 590 °C. In the same manner, $(GeTe)_nSb_2Te_3$ with n = 12, 17 and 19 and the corresponding heterostructured materials with formally 1 wt% $CoGe_2$ were characterized (the weight fractions correspond to the nominal compositions of the starting materials and are represented as *e.g.* $(CoGe_2)_x$ (matrix material) in the following). The values of the index x vary to ensure the same (at least formal) weight fraction of precipitates in all heterostructured materials.

Samples with GeTe as the matrix material exhibit the α-GeTe structure type at RT, both after the initial synthesis and after additional thermal treatment during thermoelectric measurements. This holds for water-quenched as well as MS/SPS samples (Fig. S3 and S4, ESI†). Compounds $(GeTe)_nSb_2Te_3$ (n = 12, 17 and 19), both pristine and as matrix materials, exhibit average structures that correspond to the rhombohedral α-GeTe type (Fig. S5, ESI†). The pseudocubic structure described for n = 12 [69] is not detected after MS preparation. This may be due to the small grain size in contrast to that in compact ingots, which enables relaxation to rhombohedral metrics in MS flakes. After densification by SPS, including rapid cooling from 450 °C, the structure of the $(GeTe)_{12}Sb_2Te_3$ matrix corresponds to the metastable pseudocubic state (Fig. S6, ESI†), which is in good agreement with literature.[38] GST samples with n = 17 and n = 19 retain the average rhombohedral α-GeTe-type structure. After thermal treatment during thermoelectric measurements, PXRD patterns of all samples investigated show this structure type, as indicated by broadened and/or split reflections (Fig. S6

and S7, ESI†). The likely presence of vacancy ordering, which eventually may lead to van der Waals gaps, cannot be evaluated on the basis of PXRD data, since the corresponding diffraction patterns are very similar (pseudo-homometry).[70] Note that in the case of extended van der Waals gaps, the α-GeTe type only approximates the exact average structure of heavily disordered materials.

SEM-EDX measurements confirm that the composition of the different GST and GeTe matrices are in good agreement with the initial weights (Tables S3–S5, ESI†) and corresponding SEM images show heterostructured materials (example in Fig. 1). As it is typical for GeTe,[71] small amounts of Ge precipitates were observed in some SEM images of some Sb-free samples. As weight fraction of precipitates is low, their structure could not be elucidated from PXRD patterns. TEM-EDX point measurements of the cobalt germanide precipitates, however, confirm compositions of approximately Co_5Ge_7 and $CoGe_2$ (Fig. S8 and Table S6, ESI†). In addition to previously observed[58] precipitates with Co_5Ge_7-type structure (space group *I4mm*, $a \approx 7.6$ Å, $c \approx 5.8$ Å),[72] the structure and compositions of precipitates with the EDX analysis result $Co_{30.5(1)}Ge_{66.3(4)}Sb_{0.3(1)}Te_{3(2)}$ correspond to $CoGe_2$ (space group *Cmce*, $a = 10.82$ Å, $b = 5.68$ Å and $c = 5.68$ Å)[73] according to electron diffraction. The corresponding SAED patterns and tilt angles between them are given in Fig. S9 and S10, ESI.† The pseudo-tetragonal metrics often leads to twinning, which was typically observed in SAED patterns. As both Co_5Ge_7 and $CoGe_2$ precipitates are present in the heterostructured materials, the idealized stoichiometry of the precipitates slightly deviates from the nominal composition. The cobalt germanide precipitates may also contain very small amounts of Te, which most likely has no pronounced effect on their weight fraction. As GST materials exhibit a certain homogeneity range,[36] this deviation is negligible as no other types of precipitates were detected. In the following sections, all heterostructured samples are represented by their formal nominal compositions in order to avoid the repetition of this discussion.

Microstructure

In order to understand how cobalt germanide precipitates in $(GeTe)_nSb_2Te_3$ (n = 12, 17 und 19) influence thermoelectric properties, it proved important to compare the microstructure of the samples obtained by melting and water-quenching with the ones prepared by MS and subsequent SPS. In $(CoGe_2)_{0.2}(GeTe)_{17}Sb_2Te_3$ and $(CoGe_2)_{0.22}(GeTe)_{19}Sb_2Te_3$, the growth of the small grains and sub-grains of the as-cast GST matrix during thermal treatment is most likely hindered by the presence of cobalt germanide precipitates (Fig. 1 and Fig. S11, ESI†). Only these two materials have been studied in this regard, as they have the best average zT values among GST materials. Compared to MS/SPS samples, the relative effect of precipitates on the reduction of grain and sub-grain sizes is much more pronounced for water-quenched samples, where the higher-melting cobalt germanide precipitates might act as nucleation centers for the matrix material in addition to their main effect of preventing coarsening of the matrix' microstructure. In samples obtained by MS/SPS, rapid quenching during MS outweighs the effect of the precipitates and leads to a very small grain size of the matrix material. In addition, MS samples contain much smaller cobalt germanide precipitates as compared to water-quenched samples (Fig. 2). These precipitates do not coarsen significantly upon thermal treatment during thermoelectric measurements; there are no precipitates >500 nm, which frequently occur in water-quenched samples (Fig. 1 and 2). This is explained by the fact that cobalt is not solved in the GST matrix according to EDX measurements (see Tables S3 and S5, ESI†), which impedes the growth of the precipitates by diffusion through GST. This seems reasonable as Co is insoluble in GeTe.[57] Samples that contain cobalt germanide precipitates and exhibit reduced grain and/or subgrain sizes seem to be less brittle and to have higher toughness than single-phase ones. In addition to that, precipitates and small (sub-)grain sizes might also increase the hardness of heterostructured materials.[53] Both in pristine and heterostructured, and both in water-quenched and in MS/SPS samples, grains of the GST matrix exhibit the typical ''herringbone-like'' nanodomain structures (Fig. S12, ESI†). Since these are present in all GST samples, the influence of the precipitates on the herringbone structure is negligible. These domain structures are well known from GeTe-related thermoelectric materials such as $Ge_{0.9}Sb_{0.08}Ag_{0.02}Te$, $Ge_{0.88}Sb_{0.08}Ag_{0.04}Te$ and GST.[40,58] The precipitates help to stabilize the grain size of the polycrystalline matrix material by Zener pinning;[55,74] the microstructures do not change significantly during thermal cycling in physical measurements (Fig. S13, ESI†). As a result, GST samples with cobalt germanide precipitates are characterized by smaller grain sizes compared with the pristine GST materials after thermal treatment (Fig. 1).

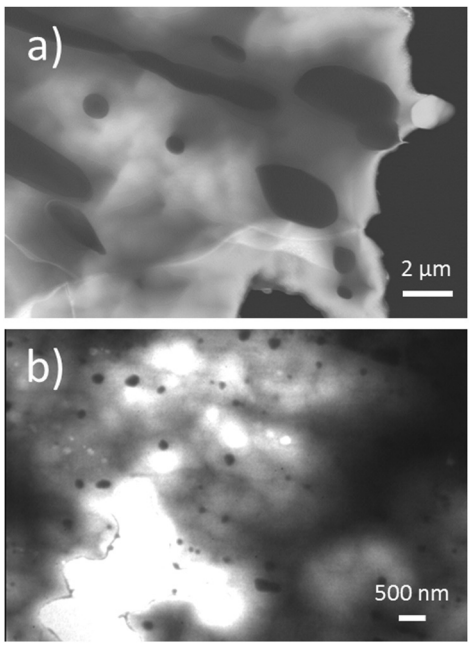

Fig. 2 (a) STEM dark field image of water-quenched and (b) TEM-BF image of MS/SPS $(CoGe_2)_{0.2}(GeTe)_{17}Sb_2Te_3$ after thermal treatment (3 cycles up to 500 °C): cobalt germanides ($CoGe_2$ and Co_5Ge_7; black spots) in $(GeTe)_{17}Sb_2Te_3$ matrix. Note that the precipitates in TEM-BF image appear dark as they are thicker than the surrounding GST matrix, which is a caused by Ar-ion-thinning.

Temperature-dependent phase transitions

Temperature-dependent PXRD (Fig. 3 and Fig. S14, ESI†) reveals phase transitions in the GeTe and GST matrices of heterostructured samples after MS/SPS. The matrix materials GeTe, $(GeTe)_{17}Sb_2Te_3$ and $(GeTe)_{19}Sb_2Te_3$ show a reversible transition between the rhombohedral α-GeTe-type at low temperatures and the rocksalt structure type at HT, both during heating (T1; Fig. 3) and cooling (T2; Fig. 3).

Quenched $(GeTe)_{12}Sb_2Te_3$, however, exhibits a pseudocubic structure at RT, which transforms to a rocksalt-type high temperature structure (T1; bottom right in Fig. 3). Upon slow cooling, this sample also transforms to a distorted variant of rhombohedral α-GeTe type as average structure (T2; Fig. 3), which is in good agreement with literature.[38,69]

Phase transitions are visible because reflections of the rocksalt-type structure type split in a characteristic way. These phase transitions correlate with the hystereses in the measurements of thermoelectric properties (*e.g.* electrical conductivity, Fig. 4 and Table S7, ESI†). As the phase transition from GeTe type to rocksalt-type itself is a displacive phase transformation, these structure models represent average structures and the hystereses (Fig. 4) are caused by vacancy diffusion and element ordering during heating and cooling as reported in the literature.[75–77]

Thermoelectric properties

After a first heating step to 500 °C, which eliminates metastable states, especially concerning the vacancy distribution,[75–77] all transport properties of heterostructured GST and GeTe samples

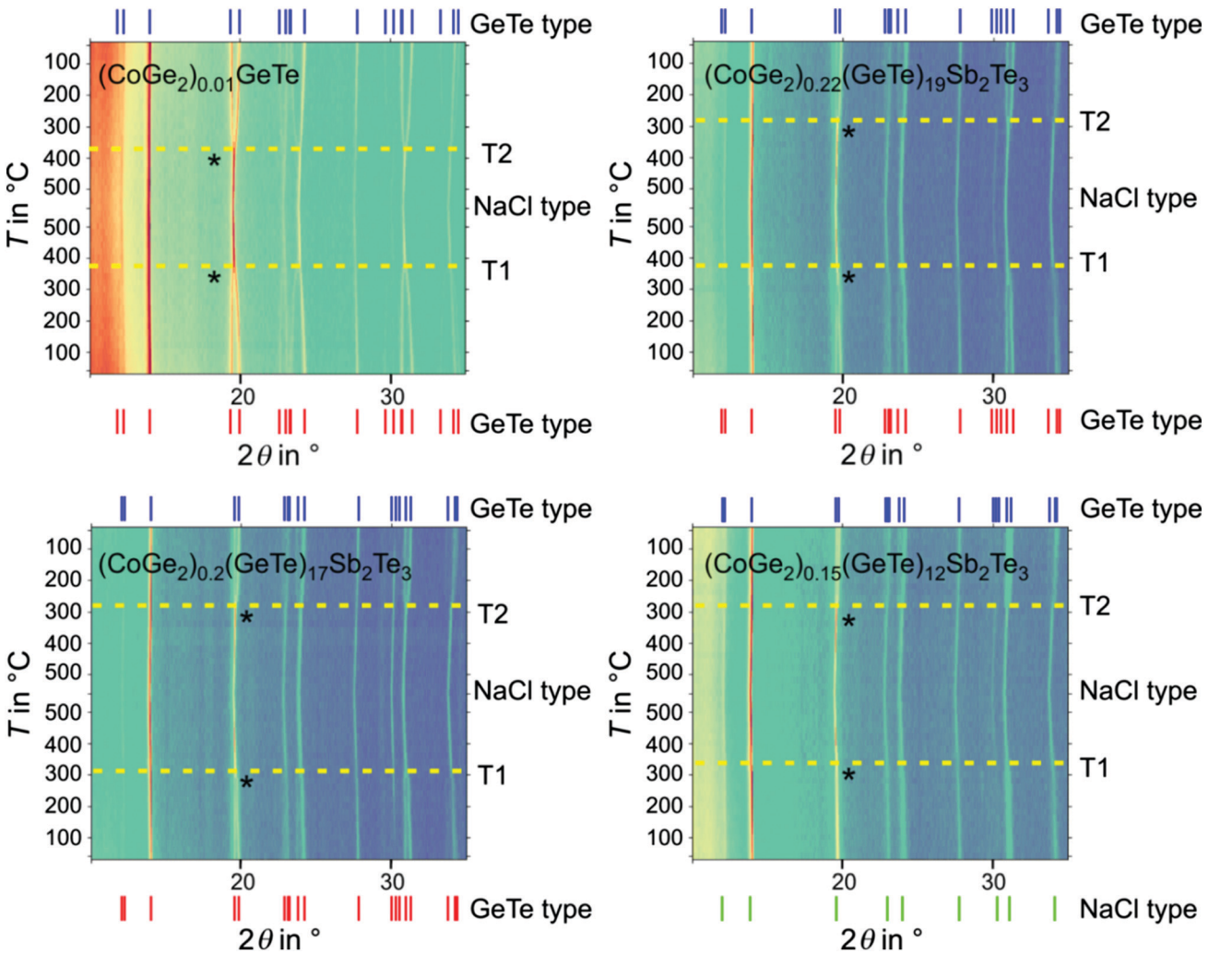

Fig. 3 Temperature-dependent PXRD of heterostructured materials with cobalt germanides with matrices of GeTe (top left), $(GeTe)_{19}Sb_2Te_3$ (top right), $(GeTe)_{17}Sb_2Te_3$ (bottom left) and $(GeTe)_{12}Sb_2Te_3$ (bottom right) as obtained by MS/SPS: at RT, the average structures of GST samples with n = 17 and 19 correspond to distorted variants of rhombohedral α-GeTe type. The GST sample with n = 12, however, exhibits pseudocubic metrics (anisotropic peak broadening indicates a very small rhombohedral distortion). Phase transitions to disordered rocksalt-type structures take place upon heating, and distorted variants of rhombohedral α-GeTe type structure are formed upon cooling in all samples. Dashed yellow lines highlight these phase transition temperatures, which are indicated by visible splitting of reflections (*e.g.* the one marked with asterisks). Red and green reflection markers, respectively, indicate the structures before heating and blue ones after cooling. Note that reflections of cobalt germanides are not visible due to their very low overall fraction.

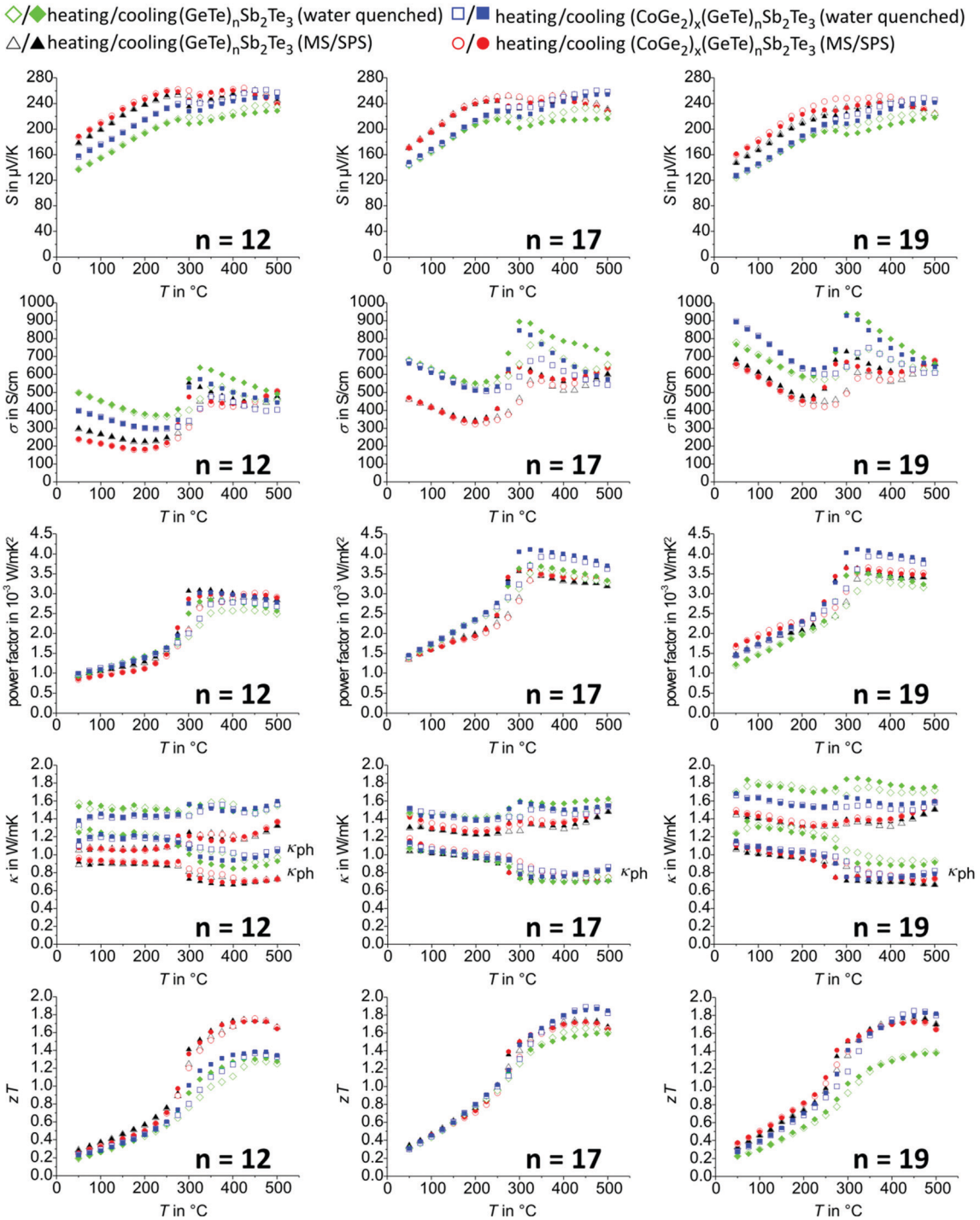

Fig. 4 Thermoelectric properties of $(GeTe)_{12}Sb_2Te_3$ *vs.* $(CoGe_2)_{0.15}(GeTe)_{12}Sb_2Te_{15}$ (left column), $(GeTe)_{17}Sb_2Te_3$ *vs.* $(CoGe_2)_{0.2}(GeTe)_{17}Sb_2Te_3$ (middle column), and $(GeTe)_{19}Sb_2Te_3$ *vs.* $(CoGe_2)_{0.22}(GeTe)_{19}Sb_2Te_3$ (right column): Seebeck coefficients (first row), electrical conductivities (second row), power factor (third row), thermal conductivities and corresponding phononic part ($L = 1.5 + e^{(-|S|/116)}$ where L is in 10^{-8} W Ω K^{-2} and S in µV K^{-1}, fourth row), and zT values (fifth row). All data points of the MS/SPS synthesis route were merged from 3 cycles between 50 °C and 500 °C, not taking into account the first heating curve which is affected by relaxation of metastable states; the individual cycles of the MS/SPS samples with the best average zT values $(GeTe)_{19}Sb_2Te_3$ and $(CoGe_2)_{0.22}(GeTe)_{19}Sb_2Te_3$ are presented in Fig, S13 und S14, ESI;† note that red dots and black triangles often overlap (especially at n = 17), as they exhibit similar values.

with cobalt germanide precipitates remain stable over several cycles and are well reproducible with samples from further syntheses, whereas in some corresponding pristine compounds a minimal decrease in zT value is detectable over time (see below). The temperature evolution of Seebeck coefficients and electrical conductivities exhibits hystereses associated with

phase transitions (Fig. 4 and 5, also *cf.* Section *temperature-dependent phase transitions*). In water-quenched GST samples, the cobalt germanide precipitates significantly influence the *zT* values. This is due to increased power factors and typically, most pronounced for water-quenched $(CoGe_2)_{0.22}(GeTe)_{19}Sb_2Te_{22}$, due to lower thermal conductivity of pristine GST material (Fig. 4). With respect to water-quenched GeTe samples, however, the beneficial effect of the precipitates is negligible. This could be due to the fact that the average charge carrier concentrations of GeTe samples are higher than optimal and thus a hetero-structuring approach is not very promising (see below). In addition, small amounts of Ge precipitates detected in GeTe might also reduce the influence of cobalt germanide precipitates. The precipitates have little influence on phonon scattering in water-quenched samples, most likely because their dimensions (Fig. 2 and Fig. S15 for water-quenched GeTe materials, ESI†) are not in the nanometer range. However, they influence the microstructure and lead to smaller grain and sub-grain sizes as exemplarily shown for $(GeTe)_{19}Sb_2Te_3$ and the corresponding heterostructure with cobalt germanides in Fig. 1; this seems beneficial for lower thermal conductivity. In contrast, the influence of cobalt germanide precipitates on the thermoelectric properties of MS/SPS samples is almost negligible; single-phase samples have almost the same *zT* values as the corresponding hetero-structured ones.

The thermal and electrical conductivities of MS/SPS samples are lower than those of water-quenched ones as the (sub-)grain sizes of the GST and GeTe matrix is drastically reduced because of the rapid solidification conditions of the MS process, which might also induce strain. As the small (sub-)grain sizes of MS samples outweighs the effect of the precipitates on the GST matrix material, their influence on the thermoelectric properties of GST is much less pronounced for MS/SPS samples than for water-quenched ones. Thus, the precipitates influence the thermoelectric properties in a rather indirect way. Their mere presence does not significantly contribute to phonon scattering and thus does not significantly reduce κ_{ph} even though their size is drastically reduced in MS/SPS samples. However, they influence the microstructure of the GST matrix, which explains their pronounced effect in water-quenched samples, whereas their effect cannot further enhance the beneficial effect of MS in terms of reducing the grain and/or subgrain size in the GST matrix. The cobalt germanides improve the long-term stability of the materials by stabilizing the microstructure by means of Zener pinning. Thus, the precipitates are also very beneficial in MS/SPS samples even if they do not enhance *zT*. In $(CoGe_2)_{0.22}(GeTe)_{19}Sb_2Te_3$ (MS/SPS), *zT* values remain stable in several consecutive cycles up to 500 °C (Fig. S16, ESI†), whereas in pristine $(GeTe)_{19}Sb_2Te_3$ (MS/SPS), κ increases and therefore *zT* gradually decreases upon thermal cycling (Fig. S17, ESI†). This can be explained by growing grains in pristine GST where the grain size is not stabilized by Zener pinning. Upon thermal cycling, increasing electrical and thermal conductivities and decreasing Seebeck coefficients result in slowly decreasing *zT* values.

However, the preparation of GeTe and its heterostructured variants by MS/SPS seems generally favorable in terms of *zT* value compared to corresponding water-quenched samples (Fig. 5). $CoGe_2$ and Co_5Ge_7 precipitates (and a very small fraction of Ge precipitates in GeTe samples) were detected as mentioned in Section *Phase composition and crystal structure*. Formally adding 1 wt% of Co_5Ge_7 to GeTe (nominal composition) turns out not to

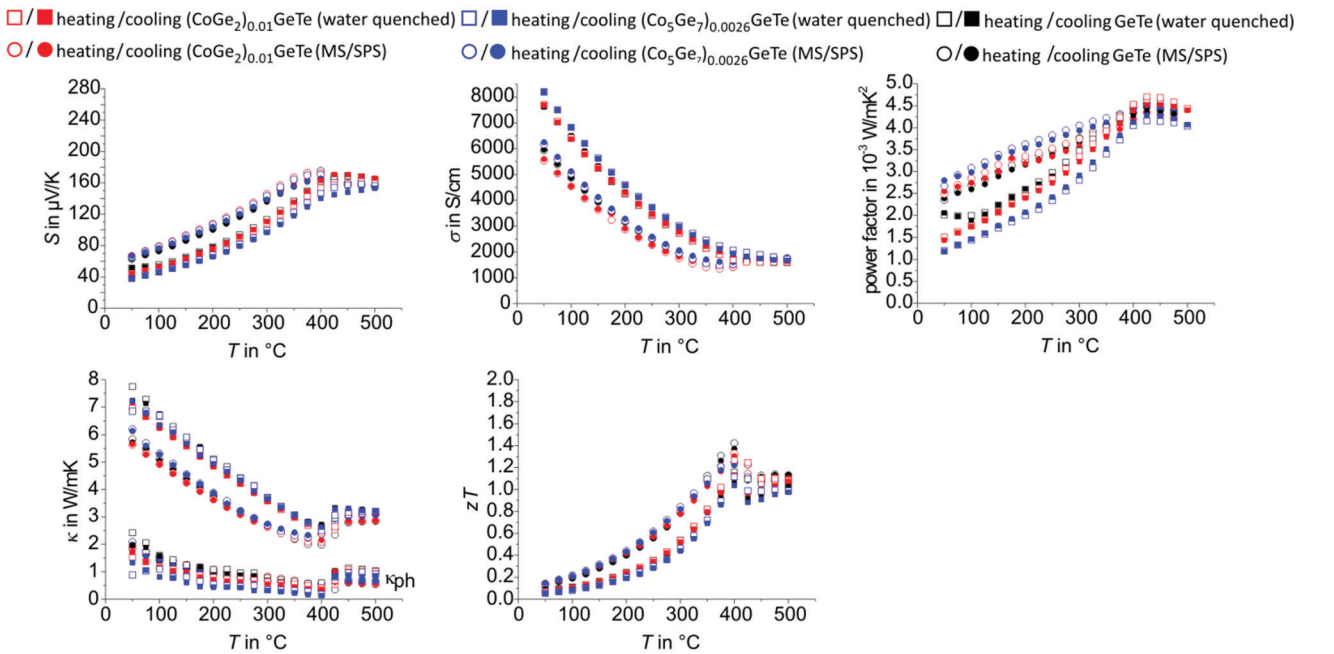

Fig. 5 Thermoelectric properties of GeTe, $(CoGe_2)_{0.01}GeTe$, $(Co_5Ge_7)_{0.0026}GeTe$; water-quenched *vs.* MS/SPS samples (*cf.* legend); Seebeck coefficient (top left), electrical conductivity (top middle), power factor (top right), thermal conductivity (bottom left), and *zT* values (bottom middle); note that squares and dots each often overlap as the measured values are similar.

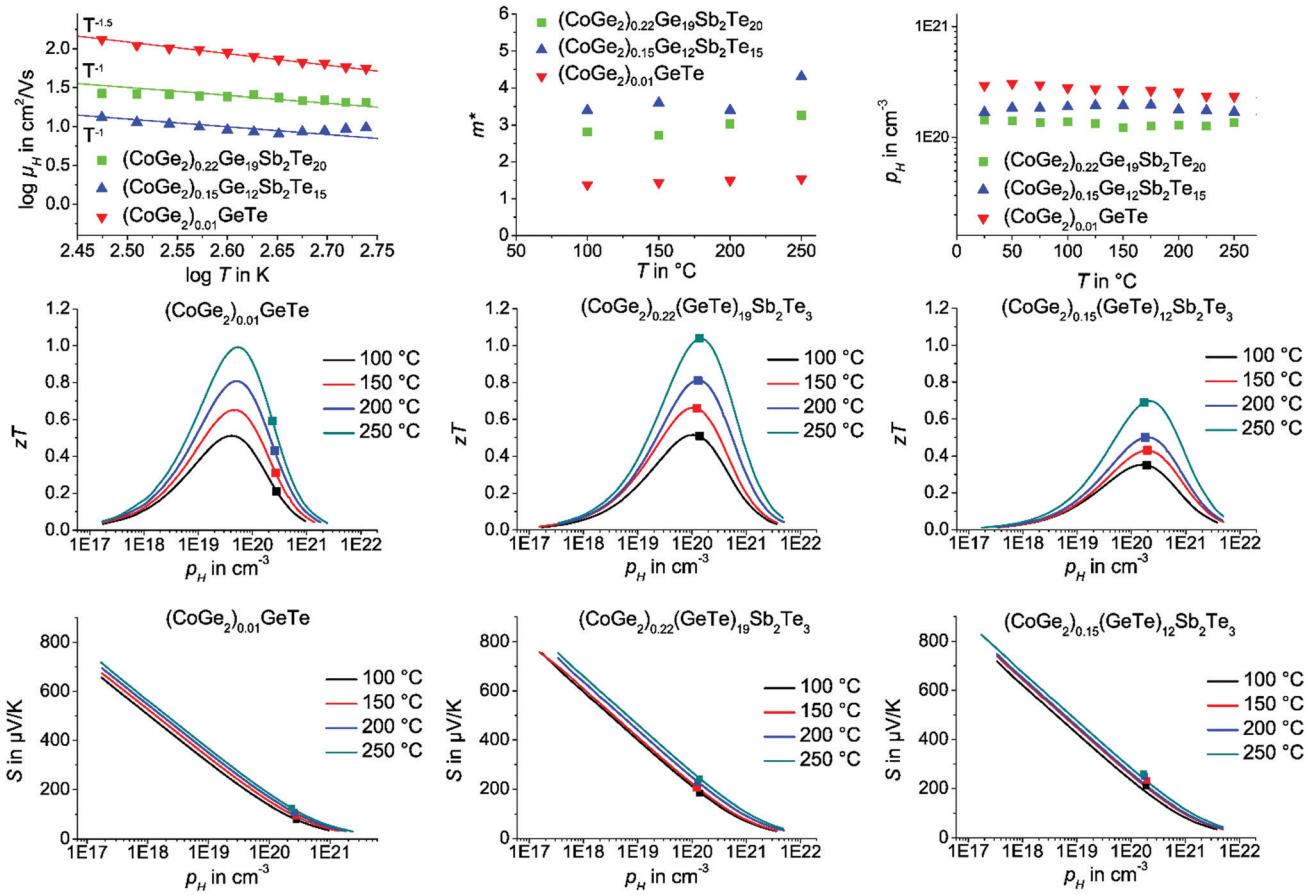

Fig. 6 Slope of the Hall carrier mobility (top left), effective mass (top middle) and the Hall carrier concentration (top right) of MS/SPS samples of $(CoGe_2)_{0.01}GeTe$ (red triangles), $(CoGe_2)_{0.15}(GeTe)_{12}Sb_2Te_3$ (blue triangles) and $(CoGe_2)_{0.22}(GeTe)_{19}Sb_2Te_3$ (green squares). For these samples, the calculated zT values as a function of p_H at 100 °C (black line), 150 °C (red line), and 200 °C (dark green) are shown (assuming SPB behavior, middle row), measured values depicted as squares; Seebeck coefficient as a function of $\log(p_H)$ (Pisarenko plot, bottom row). Details of the calculations are described at the end of the ESI† and can be found in ref. 78 and 79.

significantly influence the thermoelectric properties compared to $(CoGe_2)_{0.01}GeTe$ or GeTe. It turned out that heterostructuring GeTe with cobalt-containing precipitates is not very promising as discussed below.

The evaluation of charge carrier concentration and mobility by temperature-dependent Hall measurements gives further insights into optimal doping levels and scattering mechanisms. The application of an effective mass model (see formulae on the last page of the ESI†) reveals the theoretically possible maximum zT value for an optimal charge carrier concentration and thus the potential for further improvement *via* doping. Altogether, the approach of heterostructuring GeTe with cobalt germanides is less promising compared to GST hetero-structures, as the average carrier concentration of $(CoGe_2)_{0.01}GeTe$ is much higher than optimal. Therefore, doping GeTe would have more impact than heterostructuring. In this respect, GST can be viewed as an optimally doped variant of GeTe. The Hall carrier mobility (Fig. 6) decreases with temperature, following a relationship between $T^{-3/2}$ or T^{-1}, which would correspond to phonon scattering in non-degenerate and degenerate semiconductors, respectively. As the curves exhibit small changes in slope, the exact exponent cannot be determined reliably and one may assume an intermediate type of behavior, which is quite typical in complex alloys. Both relationships are compatible with the fact that scattering of phonons, probably both acoustic and optical, limits the charge carrier mobility.[78,79] Other forms of scattering, *e.g.* impurity scattering, would have a different temperature dependence. Therefore, the single parabolic band (SPB) model with the acoustic phonon scattering approximation was applied in the temperature range with an approximately linear increase of the Seebeck coefficient and the electrical resistivity, *i.e.* up to *ca.* 250 °C. With increasing Sb content, the Hall carrier mobility decreases. The effective charge carrier mass m^* according to effective mass modelling of all three compositions changes only very little in the temperature range from 50 °C to 250 °C and no significant changes in charge carrier concentration and mobility were detected (*cf.* Fig. 6). This confirms that the precipitates do not lead to significant changes of the matrix by mutual doping. $(CoGe_2)_{0.15}(GeTe)_{12}Sb_2Te_3$ and $(CoGe_2)_{0.22}(GeTe)_{19}Sb_2Te_3$ exhibit almost optimal charge carrier concentrations. Therefore, $(CoGe_2)_{0.22}(GeTe)_{19}Sb_2Te_3$ has the better dopant-independent intrinsic properties compared to $(CoGe_2)_{0.15}(GeTe)_{12}Sb_2Te_3$ and thus the better average zT value in the temperature range from 50 °C to 250 °C. The best performing water-quenched samples with the composition

$(CoGe_2)_{0.20}(GeTe)_{17}Sb_2Te_3$ has the same average zT value of 1.17 as $(CoGe_2)_{0.22}(GeTe)_{19}Sb_2Te_3$ (MS/SPS) – but is accessible in a more straightforward way.

Conclusions

Comparing different synthesis routes, *i.e.* water-quenching and MS/SPS, the influence of cobalt germanide precipitates in GST materials on the thermoelectric properties turned out to be rather indirect and not a simple question of phonon scattering. In MS/SPS samples, the influence of heterostructuring GST materials with cobalt germanide precipitates on the thermoelectric properties is almost negligible, even though the cobalt germanide precipitates are significantly reduced in size from ~1–2 μm (water-quenched) to <500 nm (MS/SPS). These nano-precipitates did not lead to a reduction of κ_{ph}. Therefore, it is questionable to take the effect of nano-precipitates as effective phonon scattering centers for granted without any proof. Interestingly, some other studies also reported little influence of meltspinning on thermoelectric properties. For instance, precursors prepared by melt-spinning of Bi/Sb/Te alloys did not always enhance the thermoelectric performance of Bi_2Te_3-based materials due to the rapid grain growth during SPS; and PbTe with nanoscale MgTe precipitates obtaines by MS/SPS exhibits rather similar zT values compared to corresponding ingots.[80,81]

SEM backscattered-electron orientation (''channeling'') contrast imaging with respect to the (sub-)grain size of the GST matrix material shows a significant difference in case of water-quenched samples. Introducing cobalt germanide precipitates into the GST matrix leads to an enhancement concerning thermoelectric performance of samples with microstructures that contain small grains and/or subgrains. Therefore, precipitates can be beneficial for the products of melt-casting syntheses by significantly reducing the grain, subgrain and domain sizes and would be an interesting approach for other materials to enhance their thermoelectric properties. This is especially true if the precipitates contain an element that is insoluble in the matrix, which prevents them from coarsening during annealing. Thus, Co-containing precipitates are an ideal way of heterostructuring GST materials. In MS/SPS samples, on the other hand, the grain size of the matrix material is mainly influenced by the rapid solidification conditions of MS, which leads to similar zT values of GST or GeTe and the corresponding heterostructured materials. MS/SPS samples exhibit a lower thermal conductivity, lower electrical conductivity combined with an increased Seebeck coefficient compared to water-quenched samples due to the reduced (sub-)grain size of the matrix material. In addition, heterostructuring may contribute to higher hardness (compare ref. 53) combined with an increased cyclability during thermoelectric measurements. We attribute the latter to the Zener pinning effect, which helps maintaining the (sub-)grain size of the matrix material and could be an interesting approach for future investigations in order to boost long-term stability of thermoelectric materials. As both synthesis routes lead to good thermoelectric materials, it has yet to be evaluated, which of the presented syntheses are better suited for upscaling, once these materials are considered for possible applications.

Conflicts of interest

There are no conflicts to declare.

Acknowledgements

Financial support from the European Union (European Social Fund, NFG ''Effiziente Energienutzung: Neue Konzepte und Materialien'') and the Deutsche Forschungsgemeinschaft (grant OE530/1-2) is gratefully acknowledged. S. Schwarzmüller thanks the Studienstiftung des deutschen Volkes for a fellowship. We thank, Samuel A. Miller for help with Hall measurements.

Notes and references

1 K. S. Siegert, F. R. L. Lange, E. R. Sittner, H. Volker, C. Schlockermann, T. Siegrist and M. Wuttig, *Rep. Prog. Phys.*, 2015, **78**, 013001.
2 M. Wuttig and N. Yamada, *Nat. Mater.*, 2007, **6**, 824–832.
3 T. Matsunaga, H. Morita, R. Kojima, N. Yamada, K. Kifune, Y. Kubota, Y. Tabata, J. J. Kim, M. Kobata, E. Ikenaga and K. Kobayashi, *J. Appl. Phys.*, 2008, **103**, 093511.
4 C. Rios, M. Stegmaier, P. Hosseini, D. Wang, T. Scherer, C. D. Wright, H. Bhaskaran and W. H. P. Pernice, *Nat. Photonics*, 2015, **9**, 725–732.
5 D. Lencer, M. Salinga and M. Wuttig, *Adv. Mater.*, 2011, **23**, 2030–2058.
6 J. Hegedüs and S. R. Elliott, *Nat. Mater.*, 2008, **7**, 399–405.
7 M. N. Schneider, T. Rosenthal, C. Stiewe and O. Oeckler, *Z. Kristallogr.*, 2010, **224**, 463–470.
8 D. Lencer, M. Salinga and M. Wuttig, *Adv. Mater.*, 2010, **225**, 463–470.
9 D. Samson, T. Otterpohl, M. Kluge, U. Schmid and T. Becker, *J. Electron. Mater.*, 2010, **39**, 2092–2095.
10 D. Samson, M. Kluge, T. Fuss, U. Schmid and T. Becker, *J. Electron. Mater.*, 2012, **41**, 1134–1137.
11 D. Champier, *Energy Convers. Manage.*, 2017, **140**, 167–181.
12 L. Kütt, J. Millar, A. Karttunen, M. Lehtonen and M. Karppinen, *Renewable Sustainable Energy Rev.*, 2018, **98**, 519–544.
13 X. F. Zheng, C. X. Liu, Y. Y. Yan and Q. Wang, *Renewable Sustainable Energy Rev.*, 2014, **32**, 486–503.
14 L. C. Ding, A. Akbarzadeh and L. Tan, *Renewable Sustainable Energy Rev.*, 2018, **81**, 779–812.
15 D. Beretta, N. Neophytou, J. M. Hodges, M. G. Kanatzidis, D. Narducci, M. Martin-Gonzalez, M. Beekman, B. Balke, G. Cerretti, W. Tremel, A. Zevalkink, A. I. Hofmann, C. Müller, B. Dörling, M. Coampoy-Quiles and M. Caironi, *Mater. Sci. Eng., R. Rep.*, 2018, DOI: 10.1016/j.mser.2018.09.001.
16 E. Hazan, N. Madar, M. Parag, V. Casian, O. Ben-Yehuda and Y. Gelbstein, *Adv. Electron. Mater.*, 2015, **11**, 1500228.

17 I. Cohen, M. Kaller, G. Komisarchik, D. Fuks and Y. Gelbstein, *J. Mater. Chem. C*, 2015, **3**, 9559–9564.
18 G. M. Guttmann, D. Dadon and Y. Gelbstein, *J. Appl. Phys.*, 2015, **118**, 065102.
19 Y. Sadia, Z. Aminov, D. Mogilyansky and Y. Gelbstein, *Intermetallics*, 2016, **68**, 71–77.
20 O. Appel and Y. Gelbstein, *J. Electron. Mater.*, 2014, **43**, 1976–1982.
21 P. Drude, *Ann. Phys.*, 1900, **306**, 566–613; P. Drude, *Ann. Phys.*, 1900, **308**, 369–402; P. Drude, *Ann. Phys.*, 1902, **312**, 687–692.
22 H. J. Goldschmid, *Introduction to Thermoelectricity*, Springer, Heidelberg, 2009.
23 G. Wiedemann and R. Franz, *Ann. Phys.*, 1853, **165**, 497–531.
24 H.-S. Kim, Z. M. Gibbs, Y. Tang, H. Wang and G. J. Snyder, *APL Mater.*, 2015, **3**, 041506.
25 M. M. Koza, A. Leithe-Jasper, H. Rosner, W. Schnelle, H. Mutka, M. R. Johnson, M. Krisch, L. Capogna and Y. Grin, *Phys. Rev. B: Condens. Matter Mater. Phys.*, 2011, **84**, 014306.
26 G. A. Slack, in *New Materials and Performance Limits for Thermoelectric Cooling*, ed. D. M. Rowe, CRC Press, Boca Raton, 1995, ch. 34, pp. 407–440.
27 Y. Zhang and G. D. Stucky, *Chem. Mater.*, 2014, **26**, 837–848.
28 J. B. Williams and D. T. Morelli, *J. Electron. Mater.*, 2017, **46**, 2652–2661.
29 J. B. Williams and D. T. Morelli, *J. Mater. Chem. C*, 2016, **4**, 10011–10017.
30 K. Biswas, J. He, I. D. Blum, C.-I. Wu, T. P. Hogan, D. N. Seidman, V. P. Dravid and M. G. Kanatzidis, *Nature*, 2012, **489**, 414–418.
31 K. F. Hsu, S. Loo, F. Guo, W. Chen, J. S. Dyck, J. C. Uher, T. Hogan, E. K. Polychroniadis and M. G. Kanatzidis, *Science*, 2004, **35**, 818–821.
32 J. Androulakis, K. F. Hsu, R. Pcionek, H. Kong, C. Uher, J. J. D'Angelo, A. Downey, T. Hogan and M. G. Kanatzidis, *Adv. Mater.*, 2006, **18**, 1170–1173.
33 Y. Pei, A. D. LaLonde, N. A. Heinz, X. Shi, S. Iwanaga, H. Wang, L. Chen and G. J. Snyder, *Adv. Mater.*, 2011, **23**, 5674–5678.
34 R. Hanus, M. T. Agne, A. J. E. Rettie, Z. Chen, G. Tan, D. Y. Chung, M. G. Kanatzidis, Y. Pei, P. W. Voorhees and G. J. Synder, *Adv. Mater.*, 2019, 1900108.
35 T. Rosenthal, P. Urban, K. Nimmrich, L. Schenk, J. de Boor, C. Stiewe and O. Oeckler, *Chem. Mater.*, 2014, **26**, 2567–2578.
36 R. Sankar, D. P. Wong, C.-S. Chi, W.-L. Chien, J. S. Hwang, F.-C. Chou, L. C. Chen and K. H. Chen, *CrystEngComm*, 2015, **17**, 3440–3445.
37 F. Yan, T. J. Zhu, X. B. Zhao and S. R. Dong, *Appl. Phys. A: Mater. Sci. Process.*, 2007, **88**, 425–428.
38 T. Rosenthal, M. N. Schneider, C. Stiewe, M. Döblinger and O. Oeckler, *Chem. Mater.*, 2011, **23**, 4349–4356.
39 S. Perumal, S. Roychowdhury and K. Biswas, *J. Mater. Chem. C*, 2016, **4**, 7520–7536.
40 H. S. Lee, B.-S. Kim, C.-W. Cho, M.-W. Oh, B.-K. Min, S.-D. Park and H.-W. Lee, *Acta Mater.*, 2015, **91**, 83–90.
41 S. Welzmiller, F. Heinke, P. Huth, G. Bothmann, E.-W. Scheidt, G. Wagner, W. Scherer, A. Pöppl and O. Oeckler, *J. Alloys Compd.*, 2015, **652**, 74–82.
42 T. Rosenthal, L. Neudert, P. Ganter, J. de Boor, C. Stiewe and O. Oeckler, *J. Solid State Chem.*, 2014, **215**, 231–240.
43 S. Welzmiller, F. Fahrnbauer, F. Hennersdorf, S. Dittmann, M. Liebau, C. Fraunhofer, W. G. Zeier, G. J. Snyder and O. Oeckler, *Adv. Electron. Mater.*, 2015, **1**, 1500266.
44 T. Schröder, S. Schwarzmüller, C. Stiewe, J. de Boor, M. Hoelzel and O. Oeckler, *Inorg. Chem.*, 2013, **52**, 11288–11294.
45 S. Schwarzmüller, M. Jakob, M. Nentwig, T. Schröder, A. Kuhn, A. Düvel, P. Heitjans and O. Oeckler, *Chem. Mater.*, 2018, **30**, 7970–7978.
46 F. D. Rosi, J. P. Dismukes and E. F. Hockings, *Electr. Eng.*, 1960, **79**, 450–459.
47 S. Welzmiller, R. Schlegel, A. Poppl, G. Bothmann, E.-W. Scheidt, W. Scherer and O. Oeckler, *Inorg. Chem.*, 2015, **641**, 2350–2356.
48 M. Nentwig, F. Fahrnbauer, M. Kasprick and O. Oeckler, *J. Alloys Compd.*, 2017, **694**, 1160–1164.
49 T. Rosenthal, S. Welzmiller and O. Oeckler, *Solid State Sci.*, 2013, **25**, 118–123.
50 M. Hong, Z.-G. Chen, L. Yang, Y.-C. Zou, M. S. Dargusch, H. Wang and J. Zou, *Adv. Mater.*, 2018, **30**, 1705942.
51 Y. Gelbstein, J. Davidow, S. N. Girard, D. Y. Chung and M. G. Kanatzidis, *Adv. Energy Mater.*, 2013, **3**, 815–820.
52 D. Wu, L.-D. Zhao, S. Hao, Q. Jiang, F. Zheng, J. W. Doak, H. Wu, H. Chi, Y. Gelbstein, C. Uher, C. Wolverton, M. G. Kanatzidis and J. J. He, *J. Am. Chem. Soc.*, 2014, **136**, 11412–11419.
53 M. Samanta and K. Biswas, *J. Am. Chem. Soc.*, 2017, **139**, 9382–9391.
54 X. F. Zhang, H. Terasaki and Y. Komizo, *Philos. Mag. Lett.*, 2011, **91**, 491–497.
55 R. D. Doherty, D. A. Hughes, F. J. Humphreys, J. J. Jonas, D. Juul Jenson, M. E. Kassner, W. E. King, T. R. McNelley, H. J. McQueen and A. D. Rollett, *Mater. Sci. Eng., A*, 1997, **238**, 219–274.
56 W. C. Leslie, Physical metallurgy of steels, in *Physical Metallurgy*, ed. R. W. Cahn and P. Haasen, Elsevier Science B.V., Amsterdam, 1996.
57 K. S. Kakhramoanov, M. I. Zargarova and A. A. Mageramov, *Inorg. Mater.*, 1981, **17**, 26–29.
58 F. Fahrnbauer, D. Souchay, G. Wagner and O. Oeckler, *J. Am. Chem. Soc.*, 2015, **137**, 12633–12638.
59 F. Fahrnbauer, S. Maier, M. Grundei, N. Giesbrecht, M. Nentwig, T. Rosenthal, G. Wagner, G. J. Snyder and O. Oeckler, *J. Mater. Chem. C*, 2015, **40**, 10525–10533.
60 *WINXPOW, v. 2.2.1*, Stoe & Cie. GmbH, Darmstadt, Germany, 2007.
61 A. Coelho, *TOPAS v. 5*, Coelho Software, Brisbane, 2015.
62 P. W. Stephens, *J. Appl. Crystallogr.*, 1999, **32**, 281–289.
63 *INCA, v. 4.02*, Oxford Instruments Analytical Limited, Scotts Valley, USA, 1998–2007.
64 *Genesis, v. 6.1*, EDAX, Mahwah, USA, 2010.
65 *analySIS, v. 2.1*, Olympus Soft Imaging Solutions, Münster, Germany, 1996.
66 (*a*) P. A. Stadelmann, *jEMS, v. 4.4631 U2016*, CIME-EPFL, Lausanne, Switzerland, 2016; (*b*) P. A. Stadelmann, *Ultramicroscopy*, 1987, **21**, 131–145.

67 L. Dusza, *High Temp. – High Pressures*, 1995/1996, **27/28**, 467–473.
68 K. A. Borup, E. S. Toberer, L. D. Zoltan, G. Nakatsukasa, M. Errico, J. P. Fleurial, B. B. Iversen and G. J. Snyder, *Rev. Sci. Instrum.*, 2012, **83**, 123902.
69 M. N. Schneider, P. Urban, A. Leineweber, M. Döblinger and O. Oeckler, *Phys. Rev. B: Condens. Matter Mater. Phys.*, 2010, **81**, 184102.
70 M. N. Schneider, M. Seibald, P. Lagally and O. Oeckler, *J. Appl. Crystallogr.*, 2010, **43**, 1012–1020.
71 E. M. Levin, M. F. Besser and R. Hanus, *J. Appl. Phys.*, 2013, **114**, 083713.
72 K. Schubert, T. R. Anantharaman, H. O. K. Ata, H. G. Meissner, M. Pötzschke, W. Rossteutscher and E. Stolz, *Naturwissenschaften*, 1960, **47**, 512.
73 K. Cenzual, L. M. Gelato, M. Penzo and E. Parthe, *Acta Crystallogr., Sect. B: Struct. Sci.*, 1991, **47**, 433–439.
74 G. Gottstein and L. S. Shvindlerman, in *Grain Boundary Migration in Metals: Thermodynamic, Kinetics, Applications*, ed. B. Ralph, CRC Press, Boca Raton, 2nd edn, 2009.
75 P. Urban, M. N. Schneider and O. Oeckler, *J. Solid State Chem.*, 2015, **227**, 223–231.
76 M. N. Schneider, X. Biquard, C. Stiewe, T. Schröder, P. Urban and O. Oeckler, *Chem. Commun.*, 2012, **48**, 2192–2194.
77 P. Urban, M. N. Schneider, M. Seemann, J. P. Wright and O. Oeckler, *Z. Kristallogr.*, 2015, **230**, 369–384.
78 A. F. May and G. J. Snyder, in *Thermoelectric and its Energy Harvesting*, ed. D. M. Rowe, CRC Press, Boca Raton, 2012, ch. 11, pp. 1–18.
79 S. D. Kang and G. J. Snyder, arXiv:1710.06896v2.
80 W. H. Shin, J. S. Yoon, M. Jeong, J. M. Song, S. Kim, J. W. Roh, S. Lee, W. S. Seo, S. W. Kim and K. H. Lee, *Crystals*, 2017, **7**, 180.
81 P. Eaksuwanchai, S. Tanusilp, P. Jood, M. Ohta and K. Kurosaki, *ACS Appl. Energy Mater.*, 2018, **1**, 6586.